

Effects of Domain Size and Numerical Resolution on the Simulation of Shallow Cumulus Convection

DAVID E. STEVENS

Center for Applied Scientific Computing/Atmospheric Sciences Division, Lawrence Livermore National Laboratory, Livermore, California

ANDREW S. ACKERMAN

NASA Ames Research Center, Moffett Field, California

CHRISTOPHER S. BRETHERTON

Department of Atmospheric Sciences, University of Washington, Seattle, Washington

(Manuscript received 19 November 2001, in final form 21 May 2002)

ABSTRACT

The authors present three-dimensional numerical simulations of oceanic trade cumulus clouds underlying stratocumulus clouds. The case studied is a Global Energy and Water Experiment (GEWEX) Cloud System Study (GCSS) model intercomparison that is loosely based on observed conditions during the Atlantic Trade Cumulus Experiment (ATEX). It is motivated by the importance of this cloud type to global cloud radiative forcing, and their role as a feeder system for deep convection in the Tropics. This study focuses on the sensitivity of the modeled cloud field to the domain size and the grid spacing. Domain widths from 6.5 to 20 km and horizontal grid spacings ranging from 10 to 80 m, with corresponding vertical grid spacing ranging from 5 to 40 m, are studied, involving massively parallel computations on up to 2.5 billion grid cells. The combination of large domain size and small grid resolution provides an unprecedented perspective on this type of convection.

The mean stratocumulus cloud fraction, optical depth, and vertical fluxes of heat, moisture, and momentum are found to be quite sensitive to both the domain size and the resolution. The sensitivities are associated with a strong feedback between cloud fraction, cloud-top radiative cooling, and entrainment. The properties of individual cumulus clouds rising into the stratocumulus are less affected than the stratocumulus clouds. The simulations with 80-m horizontal by 40-m vertical resolution are clearly under-resolved, with distinctly different distributions of liquid water within the clouds. Increasing the resolution to finer than 40 m horizontal/20 m vertical affects the inversion structure and entrainment processes somewhat, but has less impact on the structure of individual clouds. Large-domain simulations exhibit mesoscale structure in the cloud organization and liquid water path. This mesoscale variability feeds back on the domain-mean properties through the cloud-radiative feedback. These simulations suggest that very large computations are required to obtain meaningful cloud statistics for this case.

1. Introduction

Oceanic trade cumulus convection is an intermediate regime in the Hadley cell, which at its poleward end originates as a stratocumulus-capped boundary layer under strong large-scale subsidence. The subtropical stratocumulus to trade cumulus transition (STCT) is observed to be gradual, starting with the formation of shallow cumuli feeding into the stratocumulus clouds, followed by the breakup of the overlying stratocumulus layer (Bretherton and Pincus 1995; Wyant et al. 1997). A sizable fraction of subtropical marine stratocumulus cloud is associated with this transitional regime (Norris

1998), and contributes significantly to global cloud radiative forcing and its temporal variability (Trenberth et al. 2001).

The STCT is a challenging parameterization problem for general circulation models, due in part to an incomplete observational and conceptual understanding of turbulent mixing processes in trade cumulus clouds and how they impact the STCT. Intercomparisons of current general circulation models show that most models represent the geographical and temporal variation of this cloud type very poorly, generating large regional errors (Houghton and Meira 1995). One study that is nearly complete, the Atmospheric Model Intercomparison Project (AMIP), is the systematic intercomparison of most of the world's general circulation models. Some of the early errors detected by this project are relatively large biases in the top-of-atmosphere shortwave cloud

Corresponding author address: David E. Stevens, Lawrence Livermore National Laboratory, L-98, Livermore, CA 94551.
E-mail: stevens9@llnl.gov

radiative properties. This and other studies have stimulated recent interest in the ability of large eddy simulation (LES) models to accurately simulate the STCT.

The simulations presented here originate from a Global Water and Energy Experiment (GEWEX) Cloud System Studies (GCSS) Working Group 1 (WG1) model intercomparison described by Stevens et al. (2001). This model intercomparison, which included both LES and single-column models, focused on the regime of cumulus clouds rising into a patchy stratocumulus layer. It was based on an idealization of mean conditions observed in the Atlantic Trade Wind Experiment (ATEX) in the northeast trades in the central tropical Atlantic Ocean in February 1969 (Augstein et al. 1973, 1974; Brummer et al. 1974). Seven LES modeling groups (including ours) participated in this intercomparison and provided simulations following a strict specification.

This intercomparison was conceived in part as a comparison to a prior GCSS WG1 study of pure trade cumulus convection (Siebesma et al. 2001, manuscript submitted to *J. Atmos. Sci.*), based on large-scale conditions observed during part of the Barbados Oceanographic and Meteorological Experiment (BOMEX). In the BOMEX case, no stratocumulus clouds were observed or simulated by LES. The boundary layer was forced by a fixed profile of radiative cooling; cloud-radiation feedback was considered, but it had only minor effects. The participating LES models, run at 25-m vertical by 100-m horizontal resolution, all produced very similar statistics of cloud cover and cumulus mass flux as functions of height. One model, run at higher horizontal and vertical resolution, did produce more numerous and narrower clouds, but the profiles of cloud fraction and vertical transports were found to be insensitive to resolution (Brown 1999). The BOMEX case suggested that LES models could robustly simulate the statistics of trade cumuli at computationally reasonable grid resolutions.

In contrast, the ATEX intercomparison included a simple Beer's law feedback of cloud liquid water on radiation in addition to the specified clear-air radiative cooling. This feedback, coupled with the stronger and thinner trade inversion in ATEX than in BOMEX, greatly amplified numerical differences due to differences in the transport algorithms used. This led to large inter-model variations in the predicted stratocumulus cloud fraction and inversion deepening rate. Stevens et al. (2001) presented two sensitivity studies where one of the participating models doubled the vertical resolution and another model used 20-m resolution in all directions. The stratocumulus cloud fraction was greatly increased at the higher resolutions, in contrast to the BOMEX case.

Our study presents simulations of the ATEX case at ultrahigh (to 5 m horizontal by 10 m vertical) resolutions, and also considers the impact of using a much larger domain size (20 km) than is typical, by harnessing the power of large-scale parallel computing. Simulations

that can span the full range of length scales from that of entraining eddies to the mesoscale are ideal for designing and testing cloud parameterizations for large-scale models. Prior LES simulations have often used domains a few kilometers wide. The larger domain size considered here is comparable to the grid resolution of a typical current mesoscale model (a similar resolution will soon be achieved in some global weather forecast models), and can better represent the potential horizontal variability achievable within a mesoscale grid cell. Past LES studies have also tended to optimize vertical resolution at the expense of horizontal resolution. It is still debatable whether this has strong impacts on the turbulence statistics of the flow; certainly it provides less realistic simulation of entrainment and mixing processes involving small eddies on the scale of the vertical grid spacing.

In section 2, we describe the numerical method and turbulence model. In section 3, we discuss our simulations, followed by a summary and conclusions in section 4.

2. Model description

The model used in this study integrates a modified form of the anelastic equations of Ogura and Phillips (1962). These equations are found by decomposing the Navier–Stokes equations into three components. For a typical variable ρ , the air density, this decomposition yields

$$\rho(x, y, z, t) = \rho_0(z) + \rho_1(z) + \rho_2(x, y, z, t), \quad (1)$$

where ρ_0 is the density profile assuming an isentropic base state with constant potential temperature θ_0 , ρ_1 is the deviation of the initial environment from this base state, and ρ_2 is the evolving dynamic component predicted by the model. After including additional forcing terms, denoted by H , this results in the system of equations

$$\begin{aligned} \frac{\partial u_i}{\partial t} = & -\frac{1}{\rho_0} \frac{\partial \rho_0 u_i u_j}{\partial x_j} - \frac{\partial \Pi}{\partial x_i} + \delta_{i3} b + \frac{1}{\rho_0} \frac{\partial \tau_{ij}}{\partial x_j} \\ & + H_{u_i}^{\text{sub}} + H_{u_i}^{\text{gw}} + H_{u_i}^{\text{Coriolis}}, \end{aligned} \quad (2)$$

$$\begin{aligned} \frac{\partial \theta_i^*}{\partial t} = & -\frac{1}{\rho_0} \frac{\partial \rho_0 u_j \theta_i^*}{\partial x_j} - \frac{1}{\rho_0} \frac{\partial}{\partial x_j} \rho_0 u_j' \theta_i^{*'} + H_{\theta_i^*}^{\text{sub}} \\ & + H_{\theta_i^*}^{\text{LS}} + H_{\theta_i^*}^{\text{gw}} + H_{\theta_i^*}^{\text{rad}}, \end{aligned} \quad (3)$$

$$\begin{aligned} \frac{\partial q_i}{\partial t} = & -\frac{1}{\rho_0} \frac{\partial \rho_0 u_j q_i}{\partial x_j} - \frac{1}{\rho_0} \frac{\partial}{\partial x_j} \rho_0 u_j' q_i' + H_{q_i}^{\text{sub}} \\ & + H_{q_i}^{\text{LS}}, \quad \text{and} \end{aligned} \quad (4)$$

$$\frac{\partial}{\partial x_j} \rho_0 u_j = 0, \quad (5)$$

where Π is the perturbation pressure p_2/ρ_0 , $\theta_i^* = (\theta_i -$

θ_0/θ_0 is a scaled liquid water potential temperature, q_i is the total water mixing ratio, and $b = g\theta_{v,2}/\theta_0$ is the buoyancy. Cloud water q_c is found by inverting Wexler's equations (Flatau et al. 1992) and precipitation is neglected. The subgrid stresses τ_{ij} and Reynolds-averaged fluxes ($u'_j q'_i, u'_j \theta'^*_i$) are computed using a Smagorinsky (1963) turbulence model. (Here a Reynolds average is denoted by an overbar and the deviation from this average by a prime, which differs from a horizontal average over the domain denoted by angle brackets.) The surface momentum fluxes are calculated from a fixed friction velocity of 0.3 m s^{-1} , and the surface fluxes of θ'^*_i and q_i are fixed at 10 and 150 W m^{-2} respectively. The horizontal boundary conditions are periodic and a rigid lid is used as the upper boundary condition.

The formulations for the interior forcings H are also described in Stevens et al. (2001). These parameterize the effects of subsidence (H^{sub}), horizontal large-scale advective tendency (H^{LS}), radiation (H^{rad}), Coriolis (H^{Coriolis}), and a sponge for absorbing gravity wave energy in the top third of the domain (H^{gw}). Subsidence and horizontal advection forcings are only applied beneath the inversion (defined as the mean height of the $q_i = 6.5 \text{ g kg}^{-1}$ contour). Subsidence forcing is computed based on a mean subsidence rate of 6.5 mm s^{-1} at the inversion, linearly decreasing toward the surface. The horizontal advective tendency of temperature varies linearly from -2 K day^{-1} at the inversion to -3 K day^{-1} at the surface. That for moisture is $-1.3 \text{ g kg}^{-1} \text{ day}^{-1}$ at all heights beneath the inversion. The radiative heating is the sum of a clear-sky radiative cooling taken to be a fixed -2 K day^{-1} everywhere below the trade inversion, and a cloud-associated Beer's law long wavelength radiative cooling proportional to the liquid water content and exponentially attenuated as the overlying liquid water path increases.

The numerical model used in this study was developed by Stevens and Bretherton (1997), who fully describe the advection scheme and time marching of the physical processes. The parallelism is implemented as a distributed memory single-level adaptation of the parallel framework developed by Rendleman et al. (2000) and tested by Stevens et al. (2002). The discretization is a forward-in-time projection method using a third-order advection scheme for both velocity and scalar advection. Stevens and Bretherton (1997) found that this advection scheme had better accuracy on several test problems than many commonly used centered-difference schemes in meteorological models. The advection scheme used in this study uses a slope-limiting procedure on thermodynamic variables q_i and θ_i , but not the velocities, to limit oscillations and non-physical under- and overshoots. The slope limiting effectively adds dissipation near underresolved gradients, which gives the advection scheme performance characteristics similar to the scheme used by Shutts and Gray (1994). This slope limiting is described in detail by Almgren et al. (1998).

The Smagorinsky turbulence model is derived from

TABLE 1. Simulation names, which are combined from the domain size (S = small, L = large) and horizontal resolution in meters. Note that $\Delta y = \Delta x$ and $NY = NX$.

Simulation	L_x (km)	NX	NZ	Δx (m)	Δz (m)
L80	20.16	252	75	80.00	40.00
L40	20.16	504	150	40.00	20.00
L20	20.16	1008	300	20.00	10.00
L10	20.16	2016	600	10.00	5.00
S80	6.40	80	75	80.00	40.00
S40	6.48	162	150	40.00	20.00
S20	6.48	324	324	20.00	10.00

the assumption that subgrid turbulent fluxes of momentum and conserved scalars are downgradient, and that subgrid kinetic energy e is in local equilibrium (Smagorinsky 1963):

$$0 = K_m \text{Def}^2 - K_h N^2 - c_\epsilon \frac{e^{3/2}}{l}, \quad (6)$$

$$K_m = c_m l e^{1/2}, \quad \text{and} \quad (7)$$

$$K_h = c_h l e^{1/2}, \quad (8)$$

which, after eliminating e , yields the momentum eddy viscosity

$$K_m = c_s^2 l^2 \text{Def} \sqrt{1 - \text{Ri}/\text{Pr}}. \quad (9)$$

Here $\text{Pr} = c_m/c_h$ is a Prandtl number, $l = (\Delta x \Delta y \Delta z)^{1/3}$ is a length scale, and $\text{Ri} = N^2/\text{Def}^2$ is a gradient Richardson number. The squared buoyancy frequency is computed following MacVean and Mason (1990) to account for the effects of evaporation and mixing (see the appendix). "Def" is the local grid-scale deformation. The nondimensional constants are $c_s = 0.25$ and $\text{Pr} = 0.4$.

3. Simulations and results

We discuss two sequences of simulations, summarized in Table 1. These sequences, which differ only in domain size, consist of simulations that double in resolution from coarse to fine. The small-domain sequence has a domain size of 6.5 km in each horizontal direction, roughly that used in the GCSS intercomparison. The large-domain sequence has a corresponding domain size of 20 km, which encompasses roughly 10 times the horizontal area of the small domain. Each sequence includes three simulations with horizontal grid spacings of 80, 40, and 20 m, and vertical grid spacing equal to half of the horizontal grid spacing. This can be compared with the GCSS specification of 20-m vertical by 100-m horizontal grid spacing, which places less emphasis on achieving high horizontal resolution. Simulation names are denoted by "S" for small and "L" for large for the domain size, followed by a number indicating the horizontal resolution used in meters. Each simulation was integrated for a period of 8 simulated hours for purposes of establishing statistically steady pro-

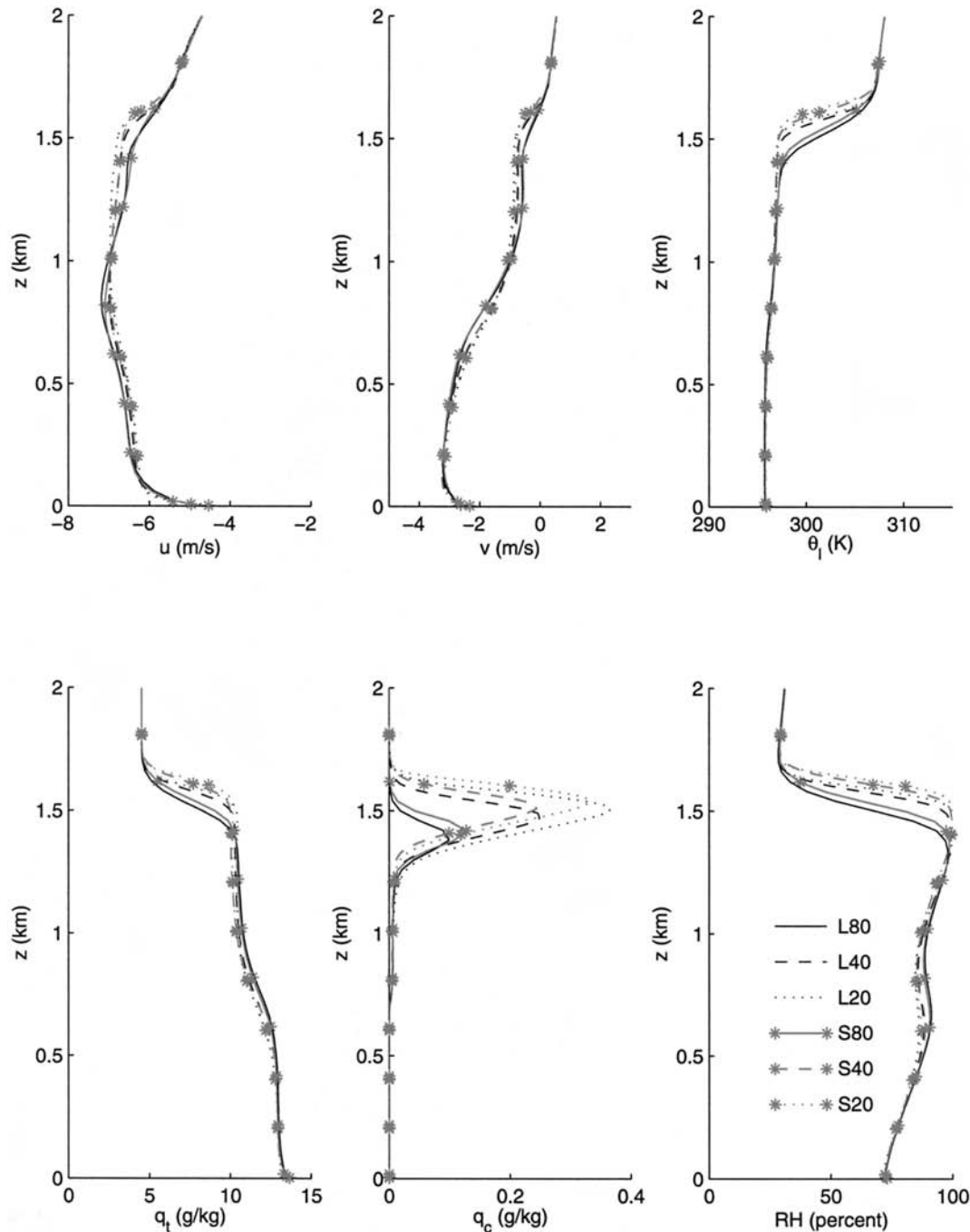


FIG. 1. Horizontally averaged profiles. These profiles are 3-h averages centered on the sixth hour of simulation.

files. The large-domain sequence also includes an ultrahigh resolution simulation L10 with 10-m horizontal by 5-m vertical resolution. L10 was spawned from the end of the seventh hour of L20 and only computed for 15 min of simulated time. Although not long enough to generate statistically stable scalar statistics and mean profiles, L10 was long enough to demonstrate changes in convective clouds and the vertical velocity spectrum. These simulations ranged in size from around 500 000 cells in the case

of S80 to 2.5 billion cells in the case of L10. L10 is the most computationally intensive simulation of cloud-topped boundary layer turbulence to date that we are aware of, using 1008 processors and 1.3 terabytes of memory to advance roughly 20 000 cells per CPU second.

Vertical profiles of the horizontal-mean velocities and thermodynamic quantities are shown in Fig. 1 for all simulations in Table 1 except L10. Like all other vertical profiles presented in this study, they are 3-h averages

over hours 5 through 7 of simulation. Over most of the boundary layer, the profiles are qualitatively similar between simulations. There is a relatively well-mixed sub-cloud layer extending up to 600 m, just below the cumulus cloud base. Above, there is a cumulus cloud layer in which the horizontal mean relative humidities are 90%–100%. The strongest vertical gradients within the cumulus layer are in the transition layer just above cloud base. An 8-K trade inversion separates the boundary layer from the drier free troposphere above. The flow is northeasterly in the boundary layer, transitioning to easterly in the cloudy layer and above.

Near the trade inversion, the differences between simulations are much more striking. At high resolution, there is a dramatic increase in condensed water q_c corresponding to the formation of a stratiform cloud layer just below the trade inversion. The inversion has risen further and is also much sharper, although this is smeared out in Fig. 1 by the time-averaging. The cloud is not associated with a boundary layer that is cooler or moister throughout. Instead it arises from the upward extension of essentially the same subinversion q_i and θ_i as in the low-resolution runs to above the associated lifted condensation level. The impact of resolution on the mean profiles is more striking than that of domain size.

Figure 2 shows the evolution of domain-averaged cloud fraction (defined as the fraction of columns containing condensate), inversion height (defined as the mean height of the $q_i = 6.5 \text{ g kg}^{-1}$ contour), liquid water path, and standard deviation of cloud water at 1500-m altitude over the entire domain. The cloud fraction increases rapidly over the first 2–3 h, exceeding 90% for the higher-resolution simulations but only 60%–70% for the lowest-resolution simulations. The inversion rise rate in the last 3 h of the simulation is close to zero for the lowest-resolution simulation, but roughly 30 m h^{-1} for the higher-resolution simulations. This reflects more entrainment of free-tropospheric air into the boundary layer with increased resolution. Similar results were presented in Stevens et al. (2001) based on a much more limited range of grid resolution. Earlier in the simulations, the entrainment rate has a strong dependence on domain size, which accumulates into a substantial height difference between corresponding small- and large-domain runs. The mean liquid water path shows the layer cloud continuing to thicken throughout the higher-resolution simulations and growing increasingly larger than in the lowest-resolution simulations, for which a nearly steady-state liquid water path is achieved. Our last statistic, the domain-mean rms q_c at 1500 m, emphasizes cloud variability. The rms q_c is roughly twice as large in each of the large-domain runs than in its corresponding small-domain run, suggestive of a mesoscale modulation of cloud liquid water.

As discussed by Stevens et al. (2001), the effect of cloud on longwave radiative cooling provides a very strong feedback in this case. More subinversion layer

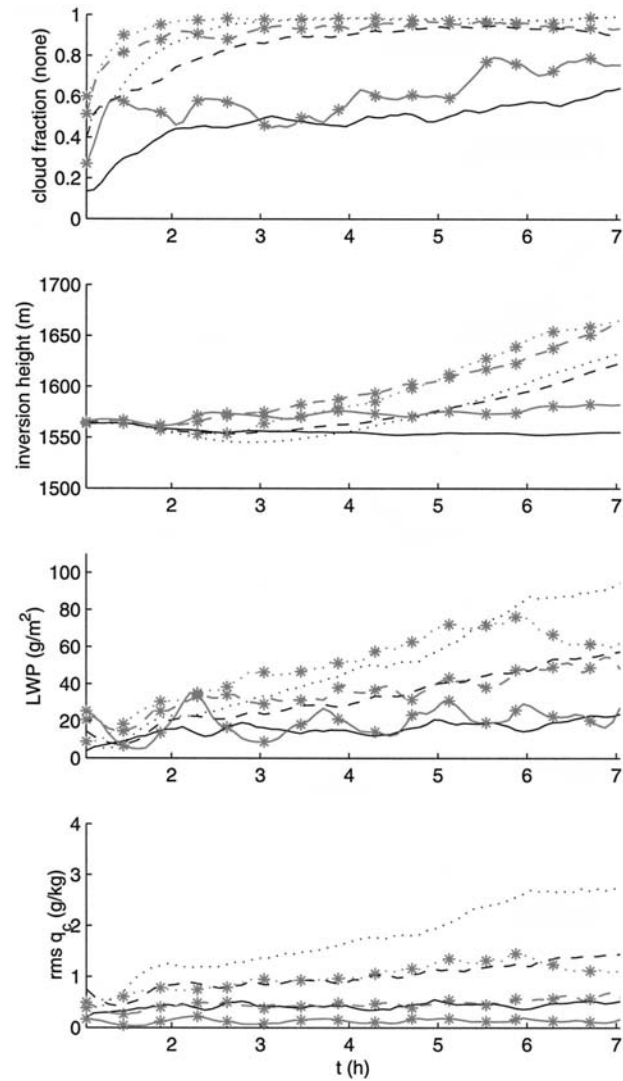


FIG. 2. Five-minute-averaged time histories of domain-averaged quantities. Line types as in Fig. 1.

cloud produces more cooling, which destabilizes the boundary layer, promotes more subinversion turbulence, more entrainment, and more cumulus convection. Small differences between our simulations are amplified by this feedback. Low-resolution simulations diffuse the inversion strongly, which inhibits cloud formation there. Any effects of domain size on layer cloud fraction will be reflected in the mean radiative cooling, the mean entrainment, and hence the evolution of all the mean profiles. A comparison summarizing the effects of resolution on the inversion height is provided in Fig. 3, which shows the entrainment rate (the rise rate of the trade inversion height minus the mean vertical velocity at that level) versus the net radiative flux divergence in the boundary layer (which is closely correlated to cloud fraction). The linearity of the relationship between the two quantities suggests that the buoyancy production

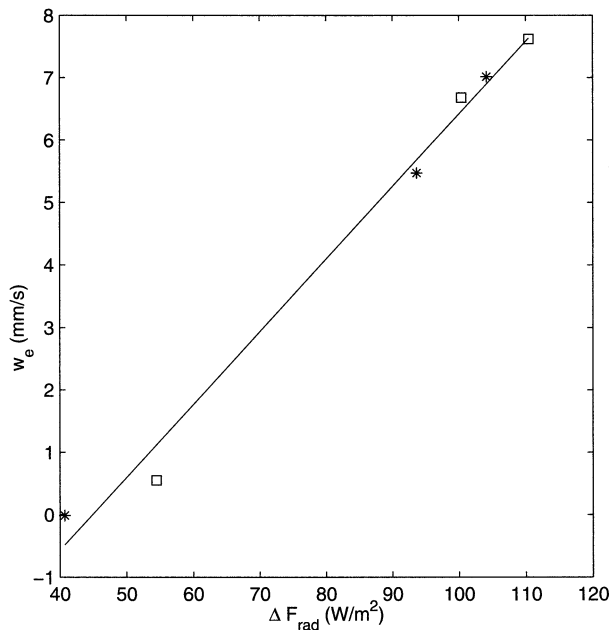


FIG. 3. Scatterplot of entrainment rate vs net radiative flux convergence. Squares and asterisks correspond to the small and large domains, respectively. Each data point is a 3-h average centered on hour 6.

produced by the radiative flux divergence cooling the cloud tops provides the turbulent kinetic energy needed to entrain inversion air. A similar relationship, but comparing different LES models instead of the same model with different resolutions and domain sizes, was seen by Stevens et al. (2001) in their Fig. 13a.

A set of vertical velocity spectra taken at 1400 m are shown in Fig. 4. These were created by averaging the periodograms of w in x over all possible values of y . The straight line is the $k^{-5/3}$ relationship, which is the expected trend for the inertial range of a turbulent cascade. The high-resolution runs, as expected, have more power at high wavenumbers. At horizontal resolutions better than 40 m a hint of an inertial range is present. Overall, the large-domain trend is similar to that observed for the small-domain sequence, but with somewhat more power observed at higher wavenumbers in the large-domain runs for coarse resolution (though S20 is indistinct from L20). The L10 simulation appears to continue the trends suggested by its coarser-resolution counterparts, suggesting that at least at high wavenumbers, the w statistics of this simulation have equilibrated with respect to any interpolation transient from its L20-derived initial condition, even after only 15 min of simulated time. All the simulations experience a fall off in the highest wavenumbers due to the Smagorinsky turbulence model; this was also seen in Brown's (1999) study and has been well-explained by Mason and Brown (1999).

Figure 5 shows horizontal cross sections of q_c for simulations L10 to L80 at a height of 1400 m, just below

the altitude of maximum stratocumulus cloud cover. All four cross sections have "mesoscale" cloud-free regions that are bigger than the entire small domain sequence of S20 to S80. As the resolution is increased, the visual appearance of the cloud field changes substantially, and in particular many more small cloud elements appear. Figure 6 zooms in on some typical convective elements indicated by the white rectangles of Fig. 5. The amount of q_c variation on length scales comparable to the grid scale is striking. In the highest-resolution run, cloud filaments of high liquid water content are closely intermingled with unsaturated dry air, reflecting the impact of small-scale mixing and entrainment.

The impact of resolution on the vertical structure of typical large convective elements is shown in Fig. 7. The low-resolution simulation L80 just resolves the main cumulus updraft, the maximum q_c is well below the cloud top due to diffusion, and there is no evidence of resolved-scale overturning at the trade inversion. L40 shows some eddy structure within an individual cumulus updraft, and maximum liquid water contents at cloud top. In L20, parts of the cloud top are overturned, indicating resolved-scale entrainment through the inversion. L10 is characterized by an even more filamentary cloud, with well-resolved turrets reflecting the influence of penetrative and lateral entrainment. From these figures, it appears that the resolution of L10 is required to produce a convincing simulation of mixing processes and liquid water statistics in individual small cumulus clouds.

Grabowski and Clark (1993) performed an elegant modeling study of three-dimensional mixing processes and buoyancy-modified shear instability at the interface of an isolated buoyant cloudy bubble and a surrounding dry environment. Their study made extensive use of grid nesting to attain resolutions of 6 m horizontally and 3 m vertically over a portion of the simulated cloud, and at the time was a computational tour de force. The computational effort of our L10 computation can be appreciated by noting that its resolution is comparable to the finest resolutions they could attain, but extends over the entirety of a 20-km horizontal, 3-km-deep domain.

Figure 8 shows a statistical perspective on the liquid water distribution of the time slices used to create the large-domain cross sections in Fig. 5. This perspective is provided at two levels: 1000 m (near the middle of the cumulus layer) and 1400 m (where cumuli are entering the base of the stratocumulus layer). This figure shows the cumulative distribution of fractional area $f(q_c)$ given by

$$f(q_c) = \frac{1}{N} \sum_{i=1}^N H(q_c(i) - q_c),$$

$$H(x) = \begin{cases} 1 & \text{if } x > 0 \\ 0 & \text{otherwise,} \end{cases} \quad (10)$$

where N is the number of mesh cells in the horizontal.

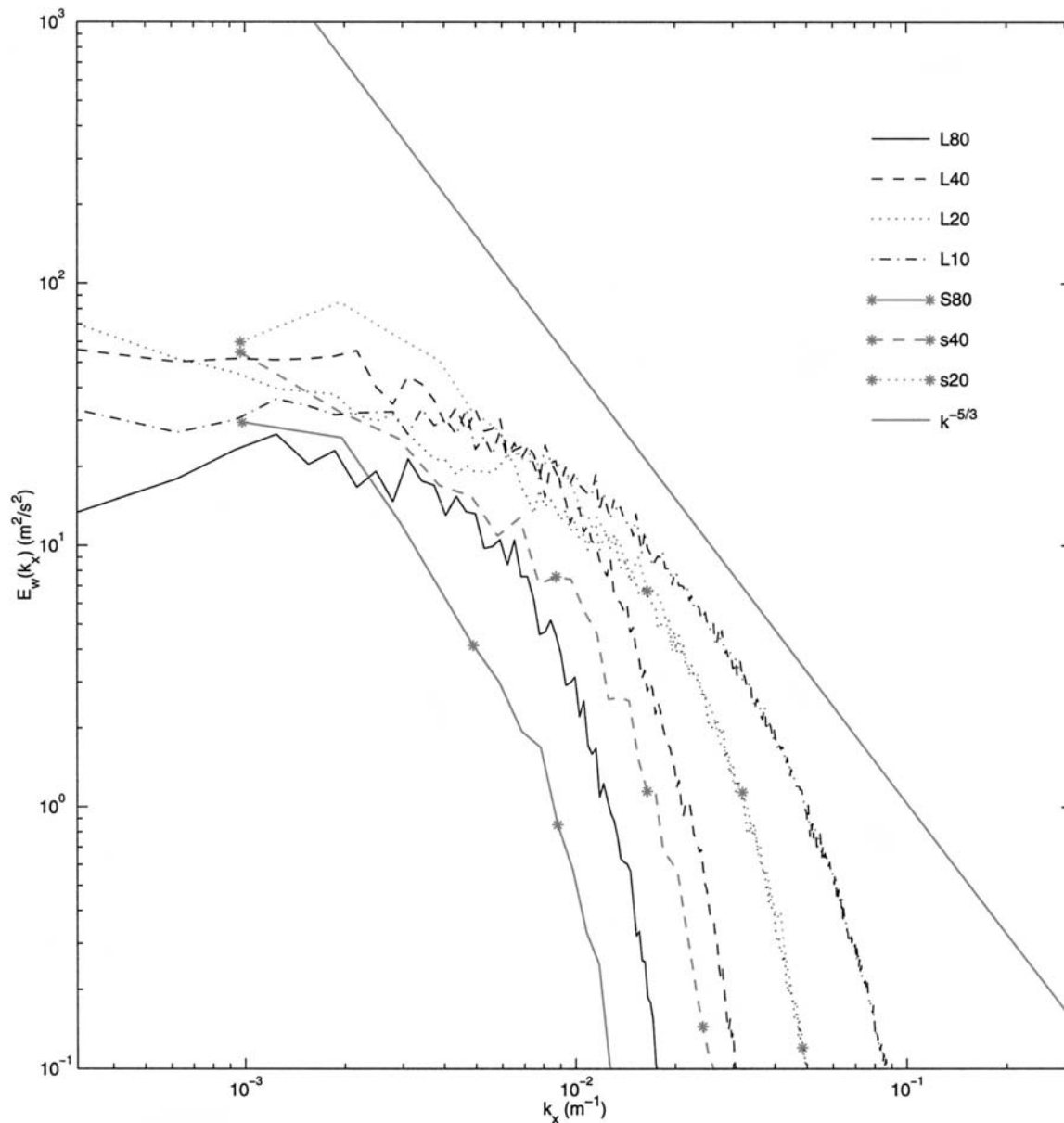


FIG. 4. Vertical velocity spectra at an altitude of 1400 m.

The shape of this curve shows the typical range of liquid water contents found in clouds at the given level. Each curve goes to zero at the maximum liquid water content found at that level, while the cumulative area fraction at $q_c = 0$ is just the cloud fraction at the given level. For the nonprecipitating clouds simulated here, this curve can be regarded as an indicator of the dilution of cloud elements by mixing between an adiabatically rising core and drier environmental air. The distribution of liquid water content is also important because it can feed back on both microphysical and radiative characteristics of the cloud.

At 1000 m, the liquid water distribution is surprisingly insensitive to resolution. We see a fairly uniform

distribution of q_c (i.e., a line of constant negative slope in the figure) between zero and 0.7 g kg^{-1} , which is the adiabatic value for undiluted air from the mixed layer. The cloud fraction at this level is between 0.02–0.03 for all resolutions. However, at 1400 m, substantial sensitivity to resolution is seen. None of the cloudy grid points at 1400 m in any simulation exceed 80% of the adiabatic value (1.1 g kg^{-1} at this altitude), indicating that substantial mixing occurs between 1000 and 1400 m. The coarse domain simulation has the lowest cloud fraction, but in half of this cloud field the liquid water content exceeds 0.3 g kg^{-1} , and 10% exceeds 0.6 g kg^{-1} . The higher-resolution simulations have a much larger cloud fraction, but less cloud area exceeding 0.3 g kg^{-1} .

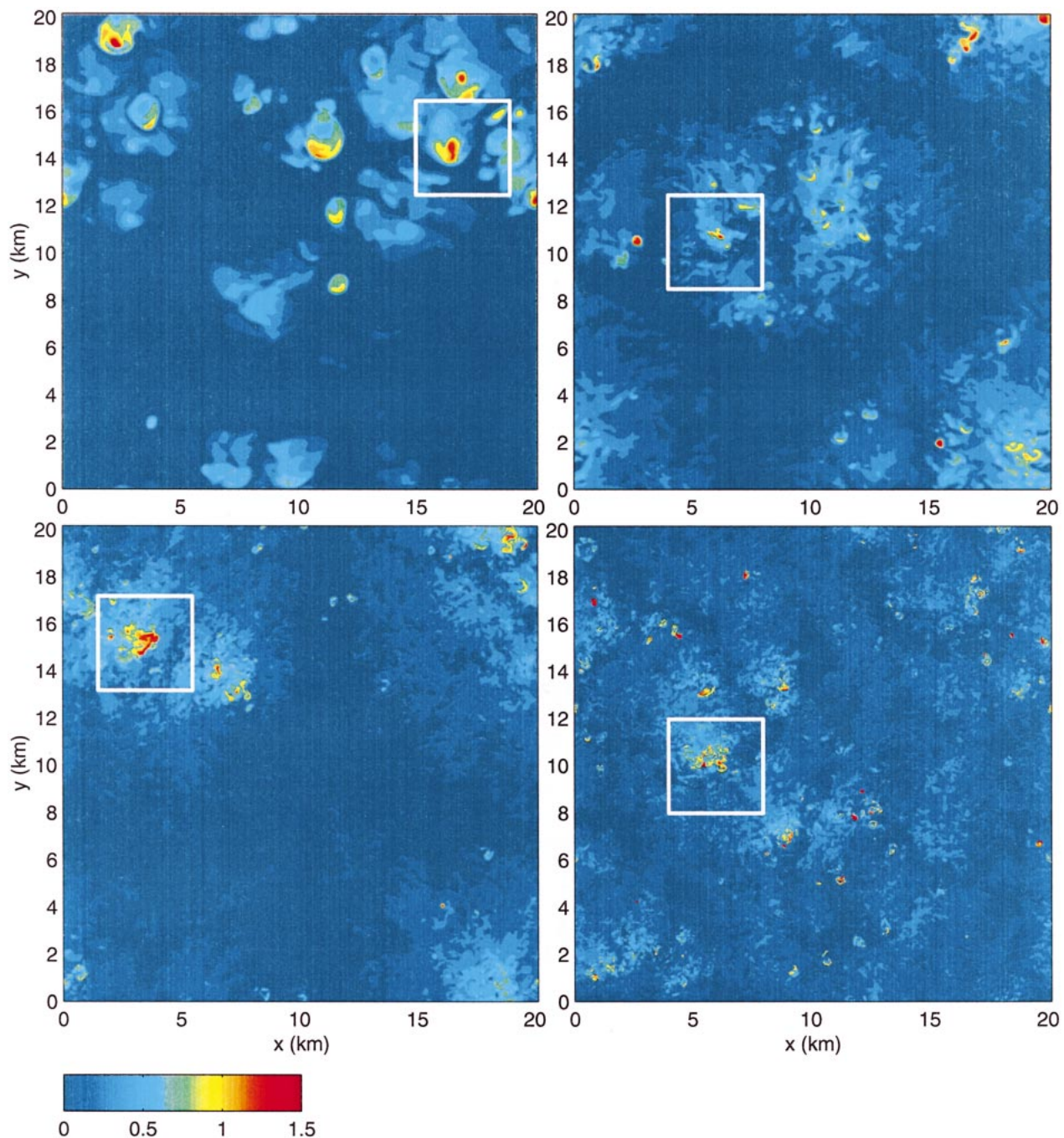


FIG. 5. Horizontal cross sections of cloud water q_c (g kg⁻¹) at an altitude of 1400 m for the entire domain, taken after 7 h of simulation. The simulations are L80 (upper left), L40 (upper right), L20 (lower left) and L10 (lower right). White boxes indicate regions where the higher-resolution cross sections of Fig. 6 are taken. The cross section from L10 was taken at 7 h, 15 min.

and less than half the cloud area exceeding 0.6 g kg^{-1} . Thus, although the overall stratocumulus cloud area increases at higher resolution, the efficiency of lateral mixing processes also appears to increase, helping to dilute the higher q_c cumulus elements. As in earlier plots, the most striking successive differences are between L80 and L40, although we caution that the spinup of L10

may not be complete after 15 min of simulation time, the time these statistics were extracted.

Horizontally averaged profiles over those regions of the domain where $q_c > 0.05 \text{ g kg}^{-1}$, denoted as cloud profiles, further elucidate changes in convective cloud structure as the resolution is increased. “Core” profiles (Siebesma and Cuijpers 1995), averaged over the same

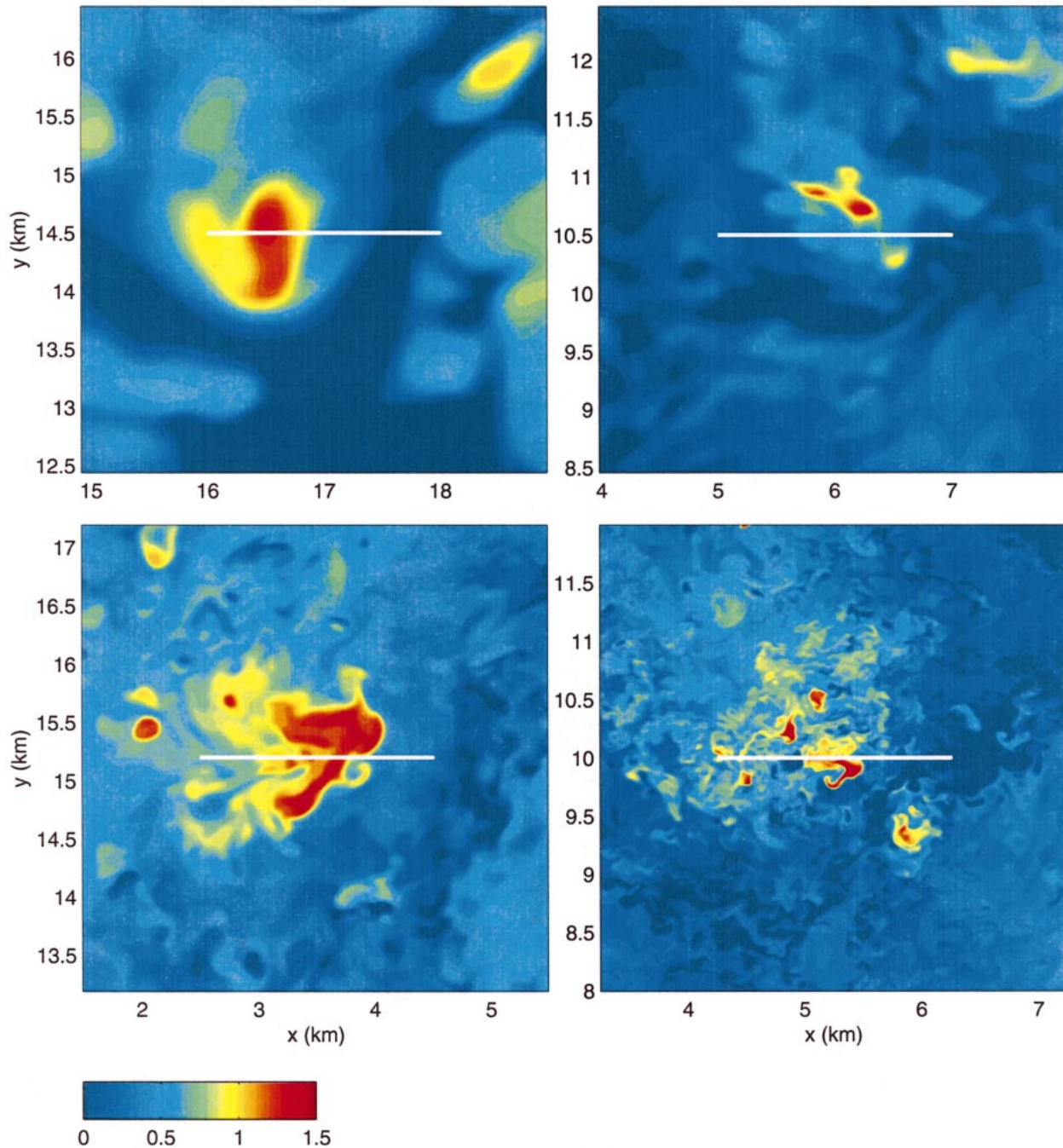


FIG. 6. Horizontal cross sections of cloud water q_c (g kg^{-1}), over the $4 \text{ km} \times 4 \text{ km}$ highlighted boxes in Fig. 5. The vertical cross sections of Fig. 7 are indicated by white lines.

cloudy regions but only including those cells which are positively buoyant compared to the domain horizontal mean, are also useful for this purpose. Figure 9 shows the profiles of cloud fraction and core fraction, and cloud-averaged vertical velocity $\langle w \rangle_{\text{cloud}}$, humidity excess $\langle q'_t \rangle_{\text{cloud}}$, and buoyancy excess $\langle \theta'_v \rangle_{\text{cloud}}$. In the cumulus layer below 1.2 km, the cloud and core fraction and the humidity and buoyancy excesses are fairly in-

sensitive to domain size and resolution. The mean in-cloud vertical velocity is systematically larger in the small-domain runs in the upper parts of the cumuli (1.1–1.3 km). Above 1.2 km, the thermodynamic excess profiles reflect stratocumulus updrafts and downdrafts as well as cumuli; differences above 1.5 km mainly reflect small negatively buoyant portions of convective cores overshooting the inversion.

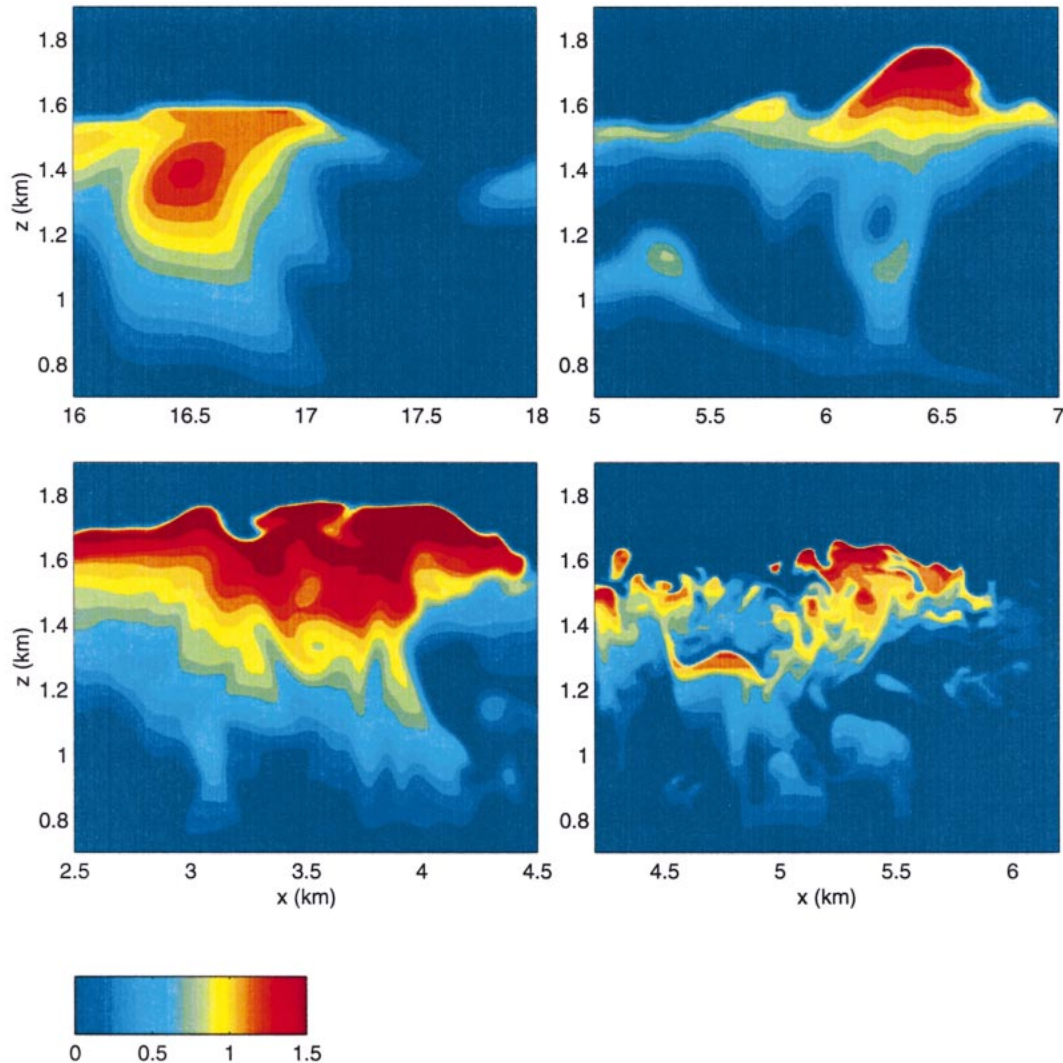


FIG. 7. Vertical cross sections of cloud water corresponding to the white lines in Fig. 6.

In Fig. 5, we saw qualitative changes in the horizontal distribution of cloudiness with increased grid resolution. This can be quantified by defining cloudy clusters—contiguous groups of cloudy cells that are completely surrounded by a 160-m-wide buffer of clear air. The buffer is a crude way to count as a single cluster a set of multiple cloud filaments that are part of a single large eddy circulation, and which may actually connect to the same cloud mass at other levels. Figure 10 shows profiles of the number density and average area of clusters. The number density of cloud clusters roughly doubles with a doubling in resolution, except for L40 and L20, which have similar number densities. There is a corresponding decrease in mean cluster area that allows the overall cloud fraction to remain fairly constant with resolution. The dip in the number density (and peak in the area) of clusters at the inversion reflects the merger that

occurs as clouds flatten out into a connected stratocumulus layer at the inversion. At the inversion, the mean cluster area approaches the domain size. The spike in cluster density just above the inversion results from the central core of many clusters overshooting the inversion.

Similar behavior in a pure trade cumulus layer was found in the simulations of Brown (1999), who investigated the role of resolution on a GCSS WG1 intercomparison case based on the BOMEX field experiment (Siebesma et al. 2001, manuscript submitted to *J. Atmos. Sci.*). As in our case, Brown found only minimal resolution sensitivity of cumulus cloud and core fraction area and cloud excesses of θ_i and q_i . Brown also found a resolution sensitivity of the cloud size distribution similar to that found here. In Brown's simulations, a factor of 3 increase in resolution decreased the area per cloud from 0.18 to 0.08 km². He hypothesized that this

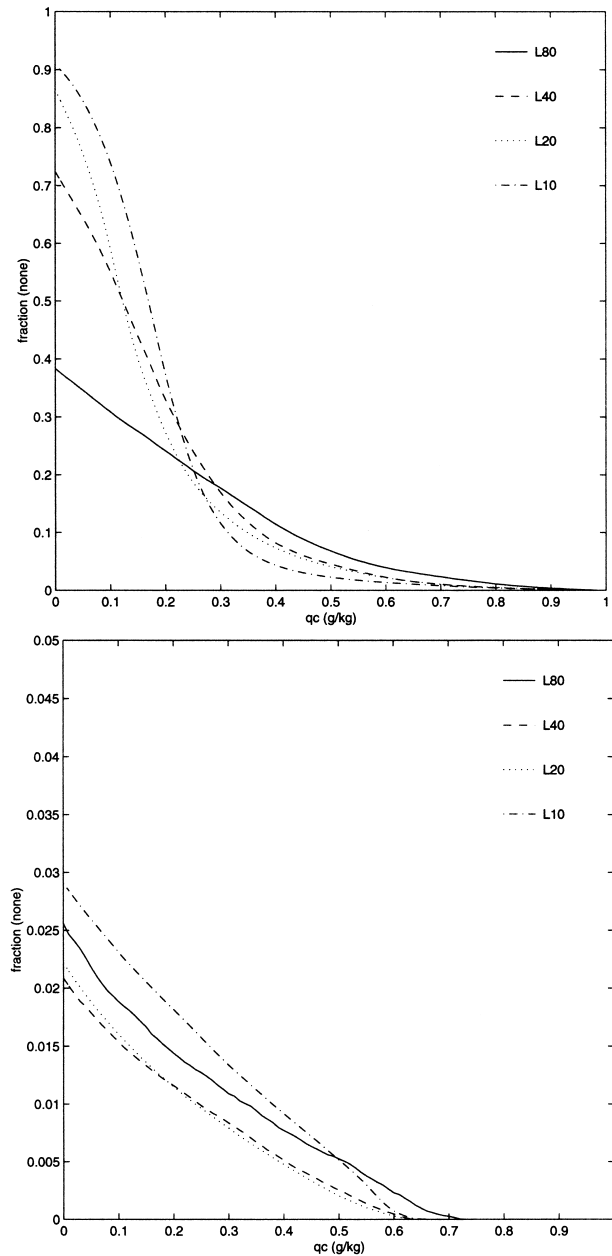


FIG. 8. Cumulative distribution of cloud water from the cross sections in Fig. 5 as defined by Eq. (10) at $z = 1400$ m (top) and $z = 1000$ m (bottom). The adiabatic value of air lifted from the well-mixed layer is roughly 0.7 g kg^{-1} at 1000 m and 1.1 g kg^{-1} at 1400 m.

resolution dependency might be due to the fact that the convective clouds are collapsing to the minimum resolution allowed by the subgrid-scale turbulence parameterization, which is typically set proportional to the grid scale.

The total flux profiles of v (crosswind momentum), θ_i , and q_i are shown in Fig. 11. These profiles can be understood as the result of differences between simulations in the cloud radiative forcing and entrainment as shown earlier. More, thicker stratocumulus cloud and

increased radiative forcing drive stronger entrainment fluxes of momentum, heat, and moisture. The individual convective elements in the lower and middle parts of the cloudy layer have transport properties that are fairly insensitive to the resolution and domain size as shown in Fig. 9. However, stronger radiative destabilization near the trade inversion supports more active convection and stronger fluxes in the finer-resolution simulations. By comparison, in Brown's (1999) BOMEX simulations, no feedback of cloud on radiation was included, and so entrainment and the heat, moisture and momentum fluxes were insensitive to resolution.

Finally, Fig. 12 shows a map of cloud albedo, derived from the liquid water path at the end of the L10 simulation assuming a constant droplet effective radius of $15 \mu\text{m}$ and an approximate formula derived from a two-stream approximation (Bohren 1987). This figure, like Fig. 5, shows several highly reflective areas that correspond to convective cores with a much higher liquid water path, detraining into stratocumulus of much lower liquid path. The details seen in this figure are strikingly similar to what is seen in high-resolution satellite photographs of cumulus convection under stratocumulus, again lending support to the unprecedented realism that can be achieved with massively parallel LES.

4. Conclusions

This study presents results from two sequences of simulations where the resolution is increased while the aspect ratio of horizontal to vertical mesh spacings is fixed at 2:1. One sequence uses a conventional domain width of 6 km ; the other uses a "large" domain width of 20 km , more capable of simulating mesoscale variability.

New scales of motion appear with each doubling of resolution. The coarsest simulation models the convection as broad homogeneous updrafts that entrain and detrain in a diffusion-like process, whereas the finest-grid simulation resolves the eddies responsible for lateral entrainment and even penetrative entrainment through the sharp, strong trade inversion. The improved resolution of the entrainment process yields different distributions of liquid water mixing ratios in the upper part of the cumuli, with the coarse domain having a relatively broad distribution and the fine domain a sharp peak in the distribution at small values.

Broadening the domain allows an upscale cascade of variance in horizontal velocity and scalar quantities, such as total water mixing ratio, promoting mesoscale organization of the cumulus convection and mesoscale variations in stratocumulus liquid water path that are similar to those seen in satellite imagery.

Changes in resolution and domain size feed back on the bulk characteristics of the boundary layer through the strong positive feedback of cloud on longwave radiative cooling in this case study. With a finer grid spacing, stratocumulus can form under the inversion without

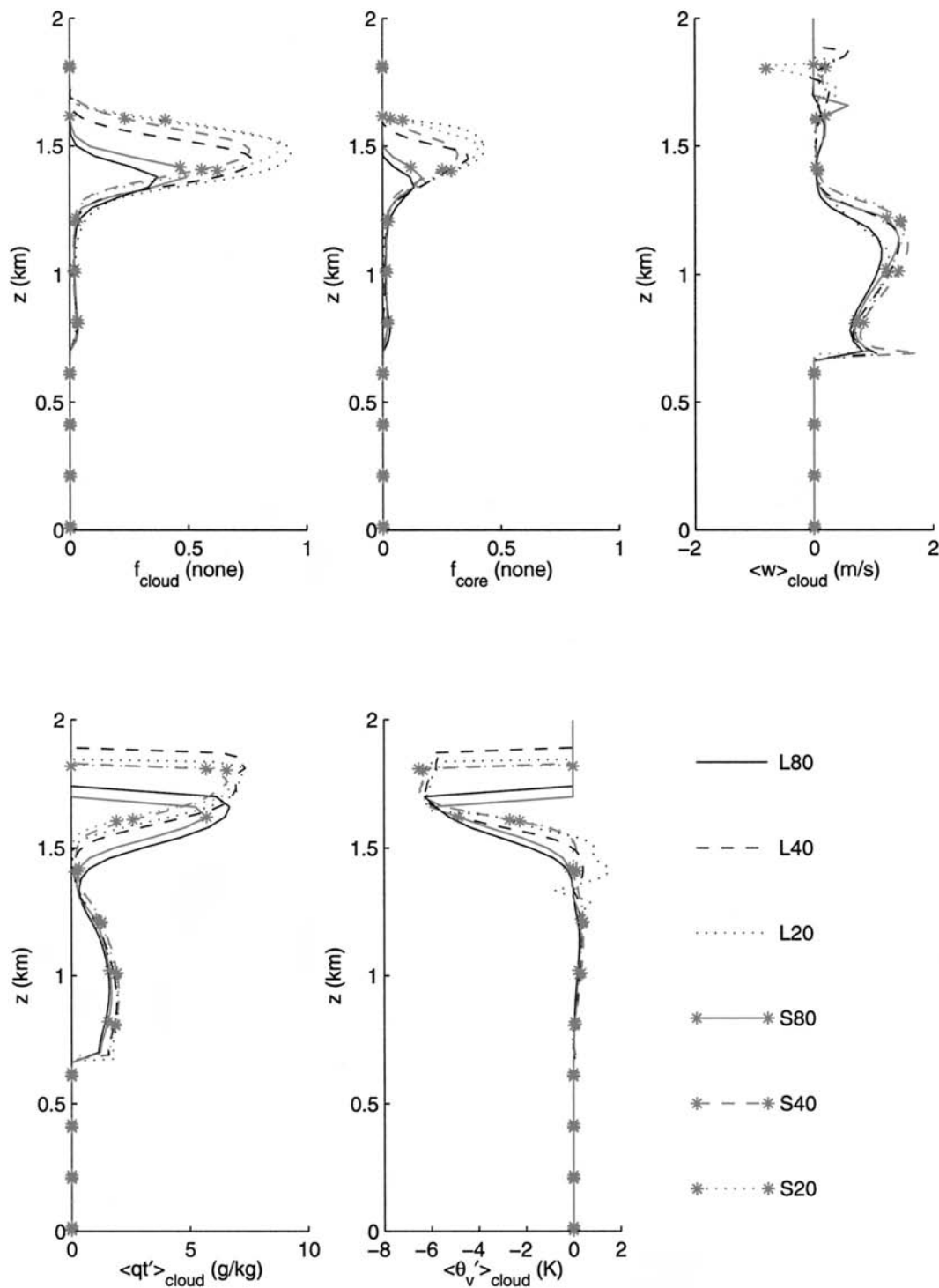


FIG. 9. Conditionally averaged cloud and core profiles: f_{cloud} is the fraction of the domain covered by cloudy grid cells and f_{core} is the core fraction; $\langle w \rangle_{\text{cloud}}$ is the cloudy mean vertical velocity, $\langle q'_t \rangle_{\text{cloud}}$ is the cloudy total water excess over the domain mean, and $\langle \theta'_v \rangle_{\text{cloud}}$ is the cloudy excess virtual potential temperature.

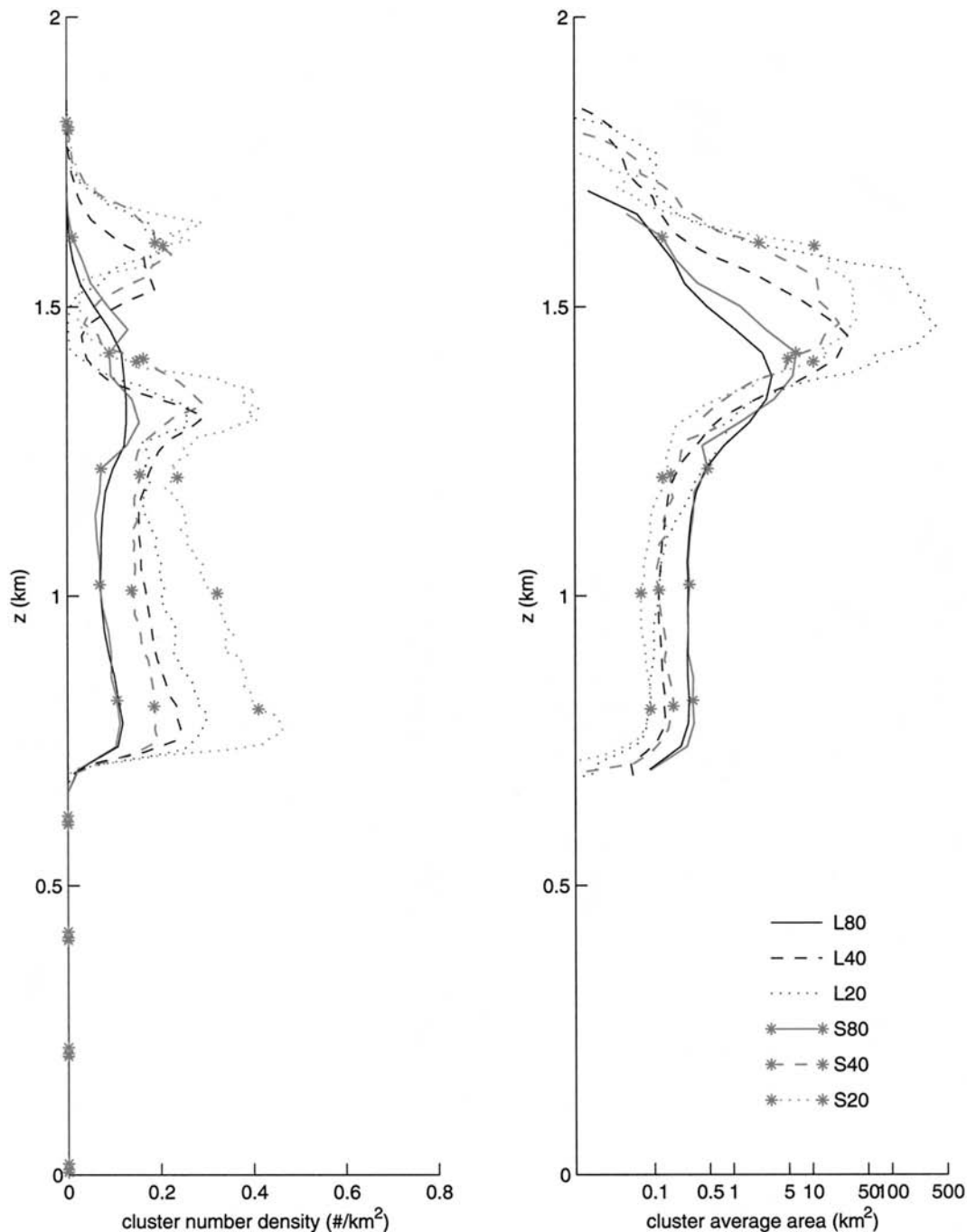


FIG. 10. The cluster number density or number of clusters per square kilometer (left), and the average area of clusters as a function of height on a logarithmic horizontal axis (right).

excessive erosion by numerical diffusion. This promotes more cloud cover, more radiative cooling, and stronger turbulence at the inversion base. This results in more entrainment, and stronger cumulus moisture and momentum fluxes. The increase in domain size was often complementary to the changes in resolution. Increased moisture and momentum fluxes were seen on the larger domain. A larger domain size effect might have been

found, if the equilibrium cloud cover were lower, in that mesoscale variability of humidity in the large-domain simulations could play an even larger role in modulating cloud cover and cloud-radiation feedbacks.

The simulations presented here are particularly relevant to the parameterization of trade cumulus convection for climate and weather prediction models, if intelligently used in combination with modern observa-

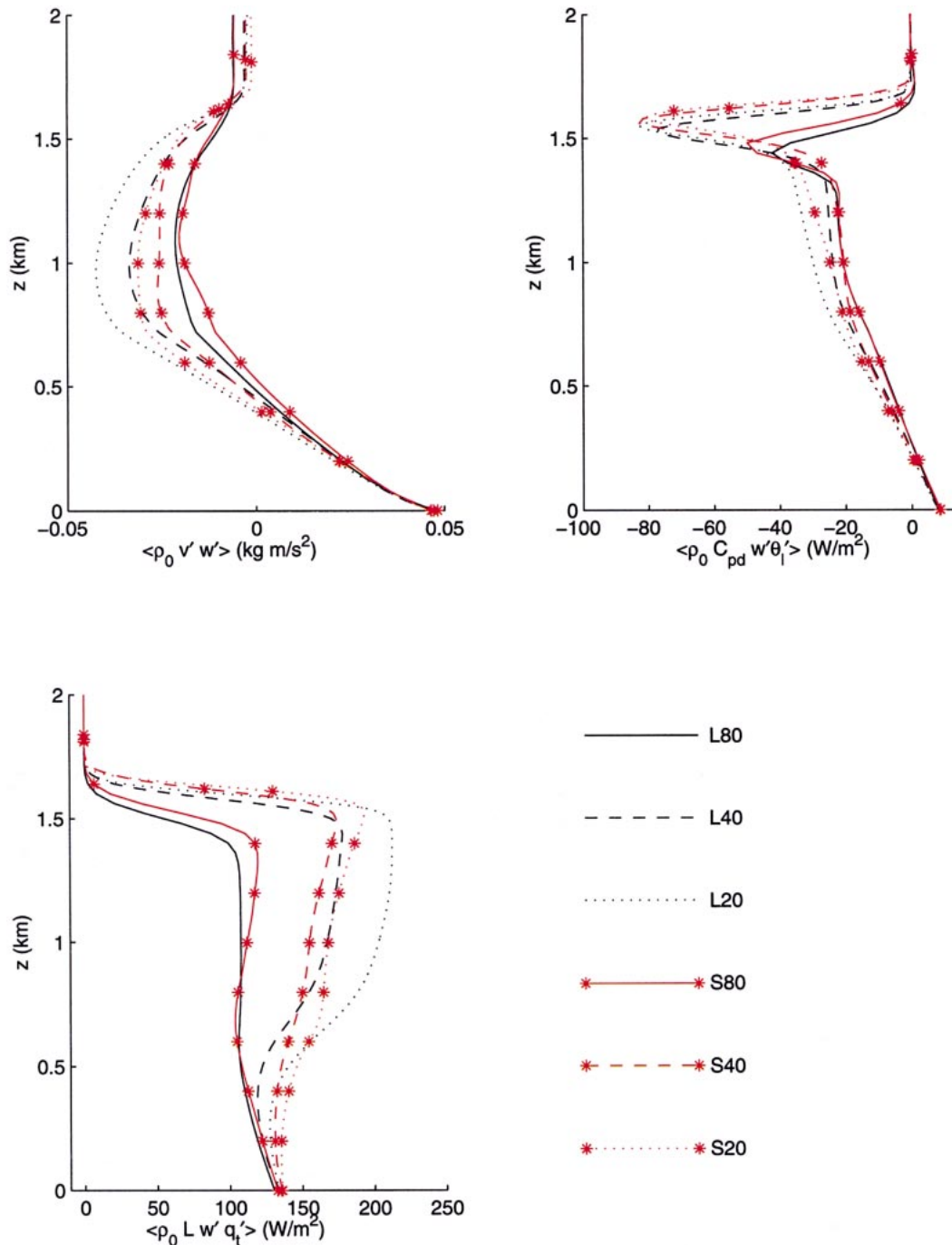


FIG. 11. Total vertical fluxes of crosswind momentum (top left), θ_l (top right), and q_l (bottom left).

tional datasets. The simulation L10 computes trade cumulus convection on a 20-km-wide square at a resolution that captures both very small-scale entraining motions and some hint of a mesoscale. In fact, several global weather forecast models will soon achieve grid spacings of 20 km, resolving the remainder of the mesoscale.

The primary goal of this study is to investigate the

turbulent dynamics that one can only resolve at very high resolutions and large domain sizes. Our study has found several sensitivities that result from altering these two factors. However, it is still premature to define definitive rules about the resolution requirements for the accurate simulation of trade cumulus convection. This is partially due to the fact that trade cumulus situations with less mesoscale organization and weaker inversions

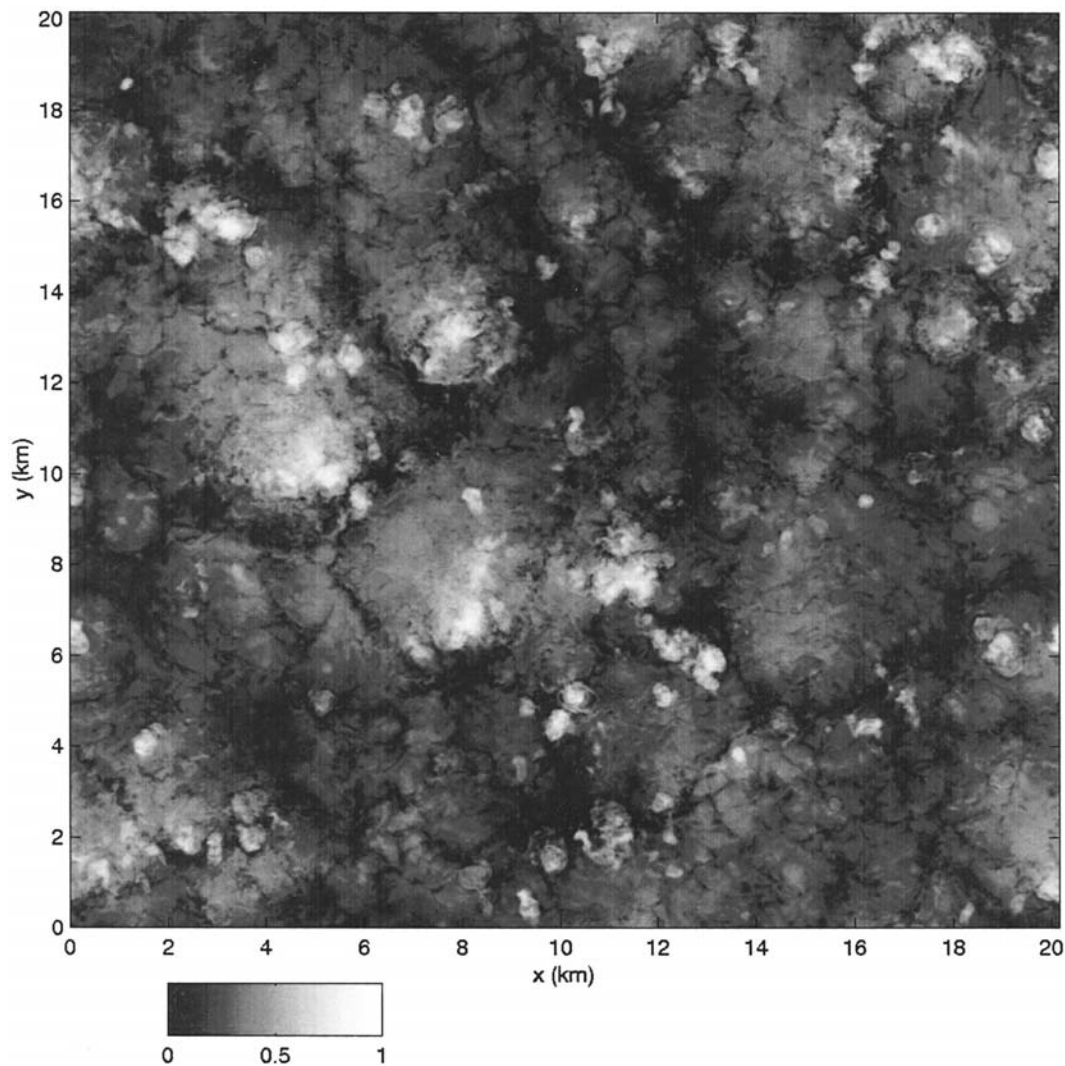


FIG. 12. Cloud albedo for L10. Bright areas indicate convective cores with a large liquid water path. These areas are typically 150 m in radius. The cores flatten at the inversion with detrainning anvils roughly 4 km wide.

require less resolution and smaller domain sizes for accurate simulation. Also, this is due to the fact that these simulations are some of the first to investigate large domain sizes at such high resolution. A more complete exploration of this parameter space will occur when this amount of computational capacity becomes available. The results from these simulations are unique in that L20 and L10 use three orders of magnitude of resolution to span the scales ranging from finescale turbulence to the lower mesoscale. More definitive rules should appear when more of these computationally intensive simulations are performed.

In pursuit of our goal of investigating cumulus convection at very high resolution, a number of simplifications have been made to the treatment of microphysical and radiative processes. This is further justified in that this study extends many of the results presented in Stevens et al. (2001) and for purposes of comparison

the treatment of these processes in our simulations strictly followed this previous study. Other simulations of this trade cumulus case (e.g., Ackerman et al. 2000) show that the effects of solar heating and precipitation can profoundly impact such fundamental properties as liquid water path and cloud coverage. An area of future work is to combine the domain size and resolution used in this study with these effects.

Acknowledgments. This work was performed under the auspices of the U.S. Department of Energy (DOE) by the University of California, Lawrence Livermore National Laboratory under Contract W-7405-Eng-48. C. Bretherton acknowledges support from NASA Grant NAGS5-10624. The results presented here would not have been possible without the assistance of many other people. We would like to thank our collaborators from the DOE Atmospheric Radiation Measurement (ARM)

Program, especially Richard Cederwall and Hung-Neng Chin, and Gerald Potter from the LLNL Program for Climate Model Diagnosis and Intercomparison (PCMDI), sponsored by the DOE Biological and Environmental Research Program. The computational support of both Lawrence Livermore and Lawrence Berkeley National laboratories were invaluable to performing these simulations. We would like to thank the staff of the LLNL Information Management Group, especially Randall Frank, Betsy Foote, and William Krauss for help with the visualization, Mark Seager and Steve Louis of the Accelerated Strategic Computing Initiative (ASCI), and the staff of the National Energy Research Scientific Computing Center (NERSC).

APPENDIX

Description of Moisture Effects on the Turbulence Model

A simple modification can be made to the Smagorinsky turbulence model to address mixing between unsaturated and saturated grid levels. The eddy viscosity in our turbulence model is influenced by the assumed balance between shear and buoyancy production, which shows up in the dependency of the eddy viscosity on the gradient Richardson number in Eq. (9). The challenge of accurately calculating the Richardson number comes from defining the stability accurately in these regions. Our modification is an extension of the work of MacVean and Mason (1990) and takes into account the changes in stability that occur when subgrid-scale mixing causes condensation (or evaporation), which can alter the subgrid-scale energy available for mixing. This modification was found during initial ATEX simulation parameter studies to significantly improve the turbulence model in regions that were stable with respect to dry convective overturning, but unstable to moist convective overturning.

Our modification of the Richardson number is derived by considering a theoretical model of two layers that start and end with well-mixed properties. The Richardson number in this model is defined to be the ratio of buoyancy production to shear production when a fixed fraction ϵ of each of two layers (subscript 1 and 2) is mixed. This yields

$$S_{\text{prod}} = -K_m \text{Def}^2/2 \quad (\text{A1})$$

$$B_{\text{prod}} = \overline{w'b'}_{\text{avg}} \quad (\text{A2})$$

$$= \frac{K_h}{4\epsilon\Delta z} [(b_2^* - b_2) - (b_1^* - b_1)], \quad (\text{A3})$$

where b_2^* is the final state of the buoyancy in layer 2 that originates as b_2 , and Δz is the thickness of each layer. The expression for the buoyancy production is derived by using the well-mixed assumption to constrain the average buoyancy flux as a piecewise linear profile that is continuous at the interface, but discontinuous

there in slope. Note that the shear production driving the mixing and the consumption of this energy by the buoyancy production are both proportional to the eddy viscosity, which thus disappears in the Richardson number as it is ratio of the two. This ratio links subgrid-scale shear production to a fixed proportional amount of subgrid-scale buoyancy production.

Were the buoyancy b conserved in the mixing process as it is in dry convection, the mixing fraction also disappears, since we can write

$$b_2^* = b_2(1 - \epsilon) + b_1(\epsilon), \quad (\text{A4})$$

$$b_1^* = b_1(1 - \epsilon) + b_2(\epsilon). \quad (\text{A5})$$

This yields the familiar gradient Richardson number:

$$\text{Ri} = N_{\text{eff}}^2/\text{Def}^2, \quad (\text{A6})$$

$$N_{\text{eff}}^2 = \frac{b_2 - b_1}{\Delta z}, \quad (\text{A7})$$

which is the ratio of an effective Brunt–Väisälä frequency N_{eff}^2 to the deformation.

Although in moist transformations buoyancy is not conserved, the change in buoyancy can be expressed in terms of quantities that are. The buoyancy in terms of the conserved variables q_t and θ_t and the nonconserved q_c is written as

$$b = \frac{g}{\theta_0} \left[\theta_t + \theta_0 r_m q_t + \left(\frac{L}{C_{pd}\Pi} - \theta_0(1 + r_m) \right) q_c \right], \quad (\text{A8})$$

where r_m is the ratio of the dry air and water vapor gas constants, L is the latent heat of vaporization, and C_{pd} is the specific heat of air at constant pressure. If the layer is saturated, to good approximation the Clausius–Clapeyron equation can be linearized about a reference saturation mixing ratio (q_{vs}) to yield

$$q_c = \frac{q_t - q_{vs} - \Pi \frac{dq_{vs}}{dT} (\theta_t - \theta_{\text{env}})}{1 + \frac{L}{C_{pd}} \frac{dq_{vs}}{dT}}, \quad (\text{A9})$$

which is linear in the conserved variables [where θ_{env} is the potential temperature corresponding to the temperature at which (q_{vs}) is evaluated]. We then can use Eqs. (A4) and (A5) to formulate this as a more appropriate Brunt–Väisälä frequency N_{eff}^2 :

$$N_{\text{eff}}^2 = \frac{g}{\theta_0} \left[\Delta\theta_t + \theta_0 r_m \Delta q_t + \frac{n}{2} G (\Delta q_t - F \Delta\theta_t) \right], \quad (\text{A10})$$

where n is the number of levels that are saturated, and F and G are given by

$$F = \Pi \frac{dq_{vs}}{dT}, \quad (\text{A11})$$

$$G = \frac{L/(C_{pd}\Pi) - \theta_0(1 + r_m)}{1 + \frac{L}{C_{pd}} \frac{dq_{vs}}{dT}}. \quad (\text{A12})$$

Note that this modification is computationally efficient in that one does not need to invert the nonlinear Clausius–Clapeyron equation to obtain the evaporation effect, and the functions F and G depend only on the initial environment and can therefore be precomputed. In the case of no saturation ($n = 0$), this expression collapses to that of the dry case.

REFERENCES

- Ackerman, A. S., O. B. Toon, D. E. Stevens, A. J. Heymsfield, V. Ramanathan, and E. J. Welton, 2000: Reduction of tropical cloudiness by soot. *Science*, **288**, 1042–1047.
- Almgren, A. S., J. B. Bell, P. Colella, L. H. Howell, and M. L. Welcome, 1998: A conservative adaptive projection method for the variable density incompressible Navier–Stokes equations. *J. Comput. Phys.*, **142**, 1–46.
- Augstein, E., H. Riehl, F. Ostapoff, and V. Wagner, 1973: Mass and energy transports in an undisturbed Atlantic trade-wind flow. *Mon. Wea. Rev.*, **101**, 101–111.
- , H. Schmidt, and F. Ostapoff, 1974: The vertical structure of the atmospheric planetary boundary layer in undisturbed trade winds over the Atlantic Ocean. *Bound.-Layer Meteor.*, **6**, 129–150.
- Bohren, C. F., 1987: Multiple scattering of light and some of its observable consequences. *Amer. J. Phys.*, **55**, 524–533.
- Bretherton, C. S., and R. Pincus, 1995: Cloudiness and marine boundary layer dynamics in the ASTEX Lagrangian experiments. Part I: Synoptic setting and vertical structure. *J. Atmos. Sci.*, **52**, 2707–2723.
- Brown, A. R., 1999: The sensitivity of large-eddy simulations of shallow cumulus convection to resolution and subgrid model. *Quart. J. Roy. Meteor. Soc.*, **125**, 469–482.
- Brummer, B., E. Augstein, and H. Riehl, 1974: On the low-level wind structure in the Atlantic trade. *Quart. J. Roy. Meteor. Soc.*, **122**, 1779–1798.
- Flatau, P. J., R. L. Walko, and W. R. Cotton, 1992: Polynomial fits to saturation vapor pressure. *J. Appl. Meteor.*, **31**, 1507–1513.
- Grabowski, W. W., and T. L. Clark, 1993: Cloud–environment interface instability. Part II: Extension to three spatial dimensions. *J. Atmos. Sci.*, **50**, 555–573.
- Houghton, J., and G. Meira, 1995: *SAR: The Second Assessment Report of the Intergovernmental Panel on Climate Change*. Cambridge University Press, 572 pp.
- MacVean, P. K., and P. J. Mason, 1990: Cloud-top entrainment instability through small-scale mixing and its parameterization in numerical models. *J. Atmos. Sci.*, **47**, 1012–1030.
- Mason, P. J., and A. R. Brown, 1999: On subgrid models and filter operations in large eddy simulations. *J. Atmos. Sci.*, **56**, 2101–2114.
- Norris, J. R., 1998: Low cloud structure over the ocean from surface observations. Part II: Geographical and seasonal variations. *J. Climate*, **11**, 383–403.
- Ogura, Y., and N. Phillips, 1962: Scale analysis of deep and shallow convection in the atmosphere. *J. Atmos. Sci.*, **19**, 173–179.
- Rendleman, C. A., V. E. Beckner, M. Lijewski, W. Y. Crutchfield, and J. B. Bell, 2000: Parallelization of structured, hierarchical adaptive mesh refinement algorithms. *Comput. Visualization Sci.*, **3**, 147–157.
- Shutts, G. J., and M. E. B. Gray, 1994: A numerical modeling study of the geostrophic adjustment process following deep convection. *Quart. J. Roy. Meteor. Soc.*, **120**, 1145–1178.
- Siebesma, A. P., and J. W. M. Cuijpers, 1995: Evaluation of parametric assumptions for shallow cumulus convection. *J. Atmos. Sci.*, **52**, 650–666.
- Smagorinsky, J., 1963: General circulation experiments with the primitive equations. Part I: The basic experiment. *Mon. Wea. Rev.*, **91**, 99–164.
- Stevens, B., and Coauthors, 2001: Simulations of trade-wind cumuli under a strong inversion. *J. Atmos. Sci.*, **58**, 1870–1891.
- Stevens, D. E., and C. S. Bretherton, 1997: A forward-in-time advection scheme and adaptive multilevel flow solver for nearly incompressible atmospheric flow. *J. Comput. Phys.*, **129**, 284–295.
- , A. S. Almgren, J. B. Bell, V. E. Beckner, and C. A. Rendleman, 2000: Small-scale processes and entrainment in a stratocumulus marine boundary layer. *J. Atmos. Sci.*, **57**, 567–581.
- Trenberth, K. E., J. M. Caron, and D. P. Stepaniak, 2001: The atmospheric energy budget and implications for surface fluxes and ocean heat transports. *Climate Dyn.*, **17**, 259–276.
- Wyant, M. C., C. S. Bretherton, H. A. Rand, and D. E. Stevens, 1997: Numerical simulations and a conceptual model of the stratocumulus to trade cumulus transition. *J. Atmos. Sci.*, **54**, 168–192.